

Enhanced Microwave Absorption Properties of Intrinsically Core/shell Structured $\text{La}_{0.6}\text{Sr}_{0.4}\text{MnO}_3$ Nanoparticles

Y. L. Cheng · J. M. Dai · X. B. Zhu ·
D. J. Wu · Z. R. Yang · Y. P. Sun

Received: 17 March 2009 / Accepted: 4 June 2009 / Published online: 17 June 2009
© to the authors 2009

Abstract The intrinsically core/shell structured $\text{La}_{0.6}\text{Sr}_{0.4}\text{MnO}_3$ nanoparticles with amorphous shells and ferromagnetic cores have been prepared. The magnetic, dielectric and microwave absorption properties are investigated in the frequency range from 1 to 12 GHz. An optimal reflection loss of -41.1 dB is reached at 8.2 GHz with a matching thickness of 2.2 mm, the bandwidth with a reflection loss less than -10 dB is obtained in the 5.5–11.3 GHz range for absorber thicknesses of 1.5–2.5 mm. The excellent microwave absorption properties are a consequence of the better electromagnetic matching due to the existence of the protective amorphous shells, the ferromagnetic cores, as well as the particular core/shell microstructure. As a result, the $\text{La}_{0.6}\text{Sr}_{0.4}\text{MnO}_3$ nanoparticles with amorphous shells and ferromagnetic cores may become attractive candidates for the new types of electromagnetic wave absorption materials.

Keywords $\text{La}_{0.6}\text{Sr}_{0.4}\text{MnO}_3$ nanoparticles · Core/shell structure · Microwave absorption · Electromagnetic matching

Introduction

In recent years, serious electromagnetic interference pollution arising from the rapidly expanding business of communication devices, such as mobile telephones and radar systems, has attracted great interest in exploiting effective electromagnetic (EM) wave absorption materials with properties of wide frequency range, strong absorption, low density, and high resistivity. Magnetic nanoparticles, besides it is important technical applications in magnetic refrigerators, magnetic recording, magnetic fluids [1], and biomedicine [2], can be a potential candidate for microwave absorption at high frequency over gigahertz, ascribed to the high Snoek's limit [3, 4]. Nevertheless, the relative complex permeability of metallic magnetic materials may decrease due to eddy current phenomenon induced by electromagnetic wave [5].

Recently, core/shell nanostructures have received intense attention due to their improved physical and chemical properties over their single-component counterparts [6], which are of great importance to a potentially broader range of applications in electronics, magnetism, and optics. A number of core/shell structured materials, like CdSe/ZnS [7, 8], CdS/ZnS [9], and ZnO/ZnS [10, 11] have been studied. Concerning the disadvantage of magnetic absorber, the fabrication of materials with core/shell microstructure is a promising way to solve this problem. Consequently, many core/shell structured materials with a magnetic metallic core and a dielectric shell have been investigated, in which the magnetic metallic materials act as a magnet that increases the permeability of the composites. While dielectric materials act not only as centers of polarization, which increases the dielectric loss, but also as an insulating matrix among magnetic metallic particles that reduces the eddy current loss. Several groups have reported good microwave

Electronic supplementary material The online version of this article (doi:10.1007/s11671-009-9374-y) contains supplementary material, which is available to authorized users.

Y. L. Cheng · X. B. Zhu · D. J. Wu · Z. R. Yang · Y. P. Sun
Key Laboratory of Materials Physics, Institute of Solid State Physics, Chinese Academy of Sciences, 230031 Hefei, People's Republic of China

J. M. Dai (✉)
School of Physics and Electronic Information, Huaibei Coal Industry Teachers College, 235000 Huaibei, People's Republic of China
e-mail: jmdai@issp.ac.cn

absorption properties of core/shell structured materials, such as α -Fe/Y₂O₃ [12], Fe/Fe₃B/Y₂O₃ [13], Ni/C [14], CoFe₂O₄/carbon nanotube [15]. Nevertheless, it is difficult to prepare monodispersed magnetic nanoparticles due to the small sizes and high active surface areas of nanoparticles that lead to aggregation easily. The complex fabrication process and uneasily controllable experimental parameters of preparing core/shell heterogeneous system are of great challenge for putting such nanocomposites absorber into practical applications. The particular electronic structure and unusual electromagnetic characteristics of the nanocrystalline perovskite manganite indicate that it has high application as microwave absorption materials. Though several works have reported the microwave absorption properties of bulk manganites [16–19], the excellent microwave absorption properties originating from the intrinsically core/shell structured nanoparticles are not reported as far as we know.

In our present work, we investigate the microwave absorption properties of half-metallic soft magnetic La_{0.6}Sr_{0.4}MnO₃ (LSMO) nanoparticles. Our experimental results demonstrate that LSMO nanoparticles with intrinsically core/shell structure are promising for the application to produce broadband and effective microwave absorbers.

Experimental

The La_{0.6}Sr_{0.4}MnO₃ (LSMO) nanoparticles were prepared by the traditional sol–gel method. The stoichiometric amounts of La₂O₃, Sr(NO₃)₂, and 50% Mn(NO₃)₂ solutions were used as starting materials, and La₂O₃ was converted into metal nitrates by adding nitric acid. These metal nitrates were dissolved in distilled water to obtain a clear solution. After stirred for 2 h, citric acid (the molar ratio of LSMO to citric acid is 2:1) was added with constant stirring, and then an appropriate amount of urea was added to the solution. Subsequently, the solution was evaporated to get a gel. The gel was firstly decomposed at about 250 °C for 24 h. The resulting powder was separated into several parts with equal mole and annealed at different temperatures of 700, 900 and 1100 °C for 6 h to obtain samples with different average particle sizes.

Phase analysis of the products was performed by powder X-ray diffraction (XRD) technique. Morphology observation of particles was conducted with transmission electron microscope (TEM), the detailed morphology of the nanoparticles was studied by means of a high-resolution transmission electron microscope (HRTEM) JEOL-2010 with an emission voltage of 200 kV. Infrared (IR) transmission spectra were collected at room temperature, in which KBr was used as a carrier. Magnetic properties were measured using a superconducting quantum interference device magnetometer (SQUID). The relative complex permeability

(μ_r) and the relative complex permittivity (ϵ_r) of the particle/wax composites were measured on a vector network analyzer (Agilent Technologies, HP8720ES) using transmission/reflection mode [20]. The prepared powders were mixed with wax by the ratio of 2:1 in weight and pressed into a mode to prepare the specimen, the coaxial cylindrical specimen was 3.04 mm in inner diameter, 7.00 mm in outer diameter, and 2.00 mm in thickness.

Results and Discussion

Structure and Morphology

X-ray diffraction (XRD) patterns of all the samples show single phase and free from impurities, and can be indexed to a single rhombohedral crystal structure with the $R\bar{3}C$ symmetry [shown in Figure S1]. The increase in the calcinations temperature from 700 to 1100 °C, resulting in the sharpening of the diffraction lines [inset of Figure S1], with an increase in intensity. The X-ray linewidths provide the average particle size (D) through the classical Scherrer formulation $D = k\lambda/B \cos \theta$, where k is a constant (~ 0.89), λ is the wavelength of the X-ray, B is the width of the half-maximum of the peak, and θ is the diffraction angle of the peak. The values of D are 35, 100 nm, for the 700 and 900 °C annealed samples, respectively. Scanning electron microscopy (not shown here) was used to characterize the particle size of the 1100 °C annealed sample and the corresponding particle size is 150 nm, which can be further proved in the following TEM morphology observation. The corresponding particles are labeled as S35, S100 and S150, respectively.

Figure 1 shows the morphology, size distribution, and microstructure of S35 and S150 investigated by TEM. The bright field image of S35 (Fig. 1a) shows an abundance of nearly spherical particles. By analyzing several frames of similar bright field images we get the histogram of the size distribution, as shown in the inset of Fig. 1a. We measured more than 200 nanoparticles, and the average diameter is estimated to be about 35 nm for S35 and 150 nm for S150 (Fig. 1b), which is in close agreement with the results obtained from XRD and SEM studies. Interestingly, the HRTEM image of S35 (Fig. 1c) clearly shows the core/shell structure with a crystalline core and an amorphous shell. The amorphous shell thickness is estimated as 8.7 nm. In the core (Fig. 1e), the d-spacing is about 0.376 nm, which agrees well with the separation between the (012) characteristic lattice planes. This implies that S35 has an intrinsically core-shell structure, which can be further confirmed by the infrared spectra. Contrastively, the HRTEM image of S150 (Fig. 1d) shows sharp edge of the particle, the clear lattice planes [the layer spacing of

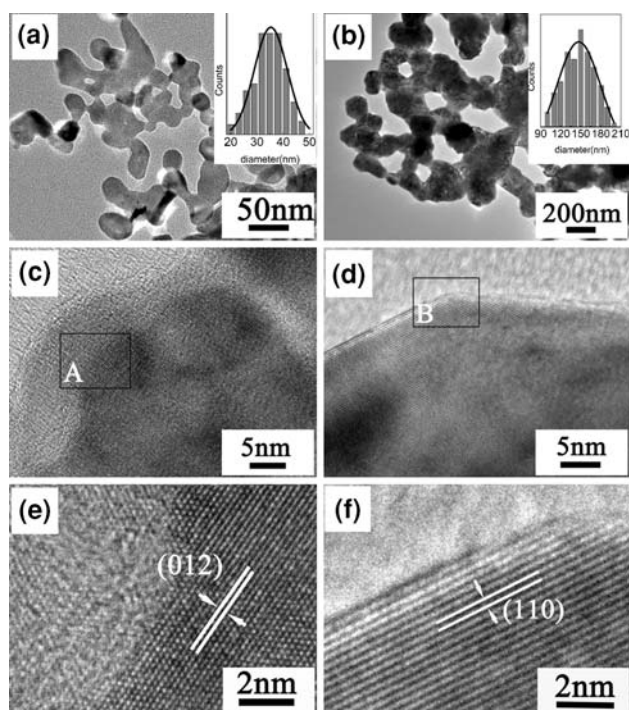


Fig. 1 TEM images of **a** S35 and **b** S150. Inset of **a** and **b** show histogram of particle size distribution of S35 and S150, respectively. HRTEM images of **c** S35 and **d** S150. Enlarged HRTEM images of **e** “A” area and **f** “B” area (Indicated by a rectangle in panel **c** and **d**, respectively)

0.274 nm, corresponding to the (110) planes] indicate the well-crystallized structure of the whole particle (Fig. 1f). The formation of amorphous shell may due to the enough low annealing temperature of the sample, which resulting in the incomplete crystallization of the surfaces of nanoparticles.

Figure 2 shows the IR transmission spectra of all studied samples. It is obvious that there is no remarkable difference between S100 and S150. The two peaks, $\nu_3 = 669 \text{ cm}^{-1}$ and $\nu_4 = 424 \text{ cm}^{-1}$, should belong to the internal phonon modes, stretching ν_3 and bending ν_4 of MnO_6 octahedra. In manganites, both ν_3 and ν_4 originate from the dynamic Jahn-Teller distortion [21, 22]. Distinctly, both the stretching ν_3 and bending ν_4 modes split into two peaks of S35. It is believed that the peak of the stretching mode at $\nu_{3s} = 592.05 \text{ cm}^{-1}$ and the one of bending modes at $\nu_{4s} = 451.26 \text{ cm}^{-1}$ should be ascribed to the surface modes [23]. The peaks at 630.62 cm^{-1} and 418.48 cm^{-1} should be still associated with stretching ν_3 and bending ν_4 modes. In addition, the peaks of ν_3 and ν_4 shift to a little lower wave number with decreasing particle size, which is thought to be a consequence of the increasing Mn–O bond length [24]. Thus, the appearance of the surface modes in S35 consists with the TEM results, which further confirms the existence of the core/shell structure in S35.

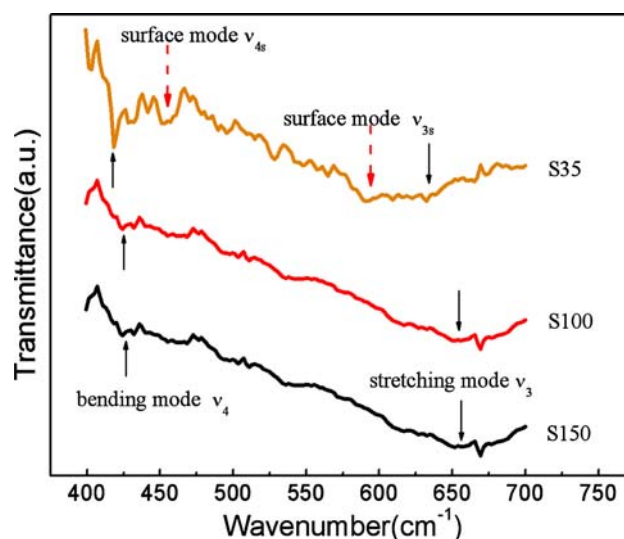


Fig. 2 IR transmission spectra of S35, S100, and S150, respectively

Magnetic and Dielectric Properties

To study the magnetic behaviors of the samples, the magnetic hysteresis loops of the samples at 300 K with different particle sizes were measured (Fig. S2). It is shown that the LSMO nanoparticles are ferromagnetic behaviors at room temperature. The inset of Fig. S2 shows the amplified image of magnetic hysteresis loop, it exhibits the soft magnetic property of prepared LSMO. The saturation magnetizations (M_s) decrease gradually with the decrease of the particle size, the values of M_s are 49, 32, and 28 emu/g for S150, S100, and S35, respectively, which are somewhat lower than that of the corresponding bulk material. For nanoparticles, the broken exchange bonds and the translational symmetry breaking of the lattice at the surfaces induce disordered spins and lead to the zero magnetization at the surface. Therefore, the increase of the relative surface contribution with decreasing particle size leads to the reduction of the M_s [25, 26]. Especially, for S35, the amorphous shell causes a greater reduction of M_s .

Figure 3 shows the frequency dependence of the relative complex permittivity and permeability of LSMO/wax compositions with different particle sizes in the range of 1–12 GHz. As shown in Fig. 3a, the real part (ϵ') and imaginary part (ϵ'') of the relative complex permittivity spectra of all the three samples have shown good dispersion relation between them and they increase slightly in the range of 1–8 GHz, and then increase strongly with the increasing frequency. It is evident that the ϵ' value of S35 is larger than that of S100 and S150 in the whole frequency range. It should relate to the existence of amorphous shell in S35. Compared with its crystallized counterpart, LSMO in an amorphous state holds more lattice defects and thus could give rise to distinct effects in mediating the electronic

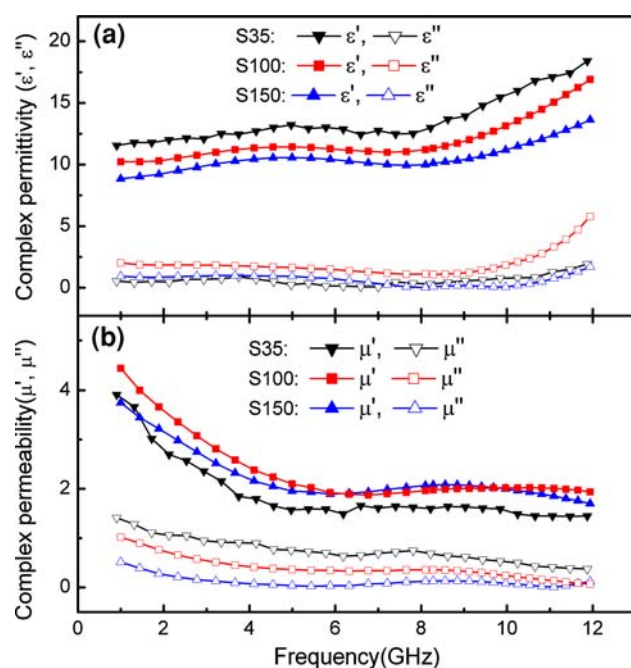


Fig. 3 Frequency dependence of **a** the relative complex permittivity and **b** the relative complex permeability of LSMO/wax compositions with different particle sizes

structure and/or tune the atomic arrangement and coordination of the outer shell [27, 28], which play a dominative role in determining the dielectric behavior of the nanoparticles. Meanwhile, the value of ϵ'' is relatively small. According to free-electron theory [29], $\epsilon'' \approx 1/2\pi\epsilon_0\rho f$, where ρ is the resistivity. It can be speculated that the lower ϵ'' values of S35 indicate a higher electric resistivity with respect to other microwave absorption materials, e.g., $\epsilon'' = 3.2 - 11.3$ for $\text{La}_{0.8}\text{Ba}_{0.2}\text{MnO}_3$ nanoparticles [30]. It may result from the small size effect and the protective amorphous shell at the surface of nanoparticles. From permittivity spectra, a dielectric resonance or relaxation phenomena are evident. This resonance may related to the matching frequency of electron hopping between Mn^{3+} -O- Mn^{4+} ions to the applied EM wave frequency. The similar result had been reported in substituted barium hexaferrites system [31]. As an anti-ferromagnetic insulator, LaMnO_3 can be transformed into ferromagnetic metal by doping Sr at A site because of double exchange mechanism [32]. When the frequency of electron hopping between Mn^{3+} -O- Mn^{4+} ions matches that of microwave, dielectric resonance phenomenon occurs, which is responsible for the increasing dielectric loss.

In Fig. 3b, it is found that both the real part (μ') and imaginary part (μ'') of the relative complex permeability spectra have shown good dispersion relation. For all the samples, with increasing frequency, both μ' and μ'' values exhibit an abrupt decrease in the range of 1–6 GHz, and

then a resonance phenomenon accompanied with a broad peak at 6–12 GHz occurs. Previous investigations [33, 34] have shown that $\text{La}_{1-x}(\text{Sr}, \text{Ba})_x\text{MnO}_3$ micro-size powders exhibited giant microwave loss at ~ 10 GHz arising from natural ferromagnetic resonances. In the present $\text{La}_{0.6}\text{Sr}_{0.4}\text{MnO}_3$ composition, the observed μ'' spectra as shown in Fig. 3b are in good agreement with the mechanism of natural ferromagnetic resonance arising from the magnetic anisotropy consequent on the strains in the grains. Additionally, it is found that the μ' values decrease, while the μ'' values increase with decreasing particle size, due to the smaller saturation magnetizations M_s of small-sized particles. It is known that μ' and μ'' values are correlated, standing for the energy storage and loss, respectively. Obviously, the inverse changes of μ' and μ'' are attributed to the magnetic properties of LSMO nanoparticles, which play an important role in determining the magnetic behavior of the composites, endowing the composites with strong magnetic loss. Magnetic loss is caused by the time lag of the magnetization vector M behind the magnetic field vector H . The change of the magnetization vector is generally brought about by rotation of the magnetization or the domain wall displacement. These motions lag behind the change of the magnetic field and contribute to μ'' . The smaller the particle size, the weaker the spins coupling at the particles' surface, which makes the magnetic relaxation behavior more complex, and will give rise to a magnetic loss mechanism. Additionally, the domain wall displacement loss occurs in multidomain magnetic materials, in LSMO nanoparticles where size is larger than the critical size for single magnetic domain (25 nm) [35], the domain wall displacement loss plays an important role in magnetic loss. Therefore, it is reasonable to deduce that the magnetic loss is due to significant contributions from both the natural ferromagnetic resonance and the domain wall displacement loss.

Microwave Absorption Properties

According to the transmission line theory, the reflection loss (RL) curves at the given frequency and absorber thicknesses were calculated as follows [36]:

$$Z_0 = Z_0(\mu_r/\epsilon_r)^{1/2} \tanh [j(2\pi fd/c)(\mu_r\epsilon_r)^{1/2}]$$

$$\text{RL} = 20 \log |(Z_{\text{in}} - Z_0)/(Z_{\text{in}} + Z_0)|$$

where f is the frequency of incident electromagnetic wave, d is the absorber thickness, c is the velocity of light, Z_0 is the impedance of free space, and Z_{in} is the input impedance of absorber.

Generally, the excellent EM-wave absorption of materials is known to result from efficient complementary

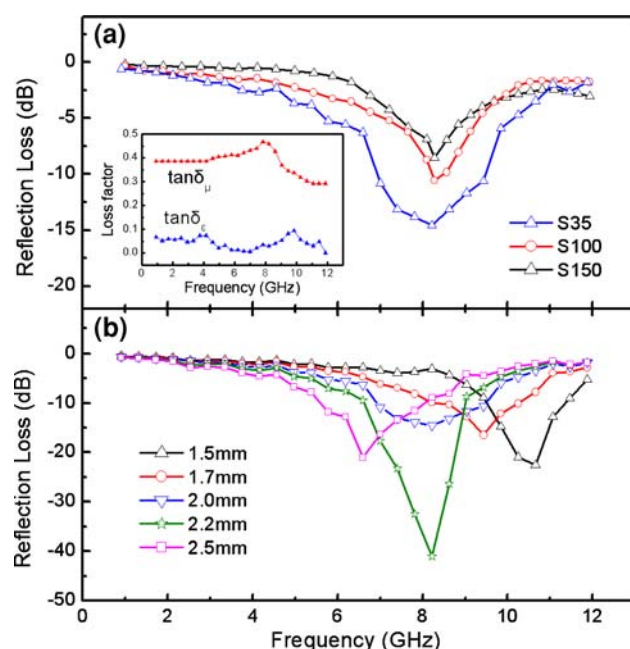


Fig. 4 Frequency dependence of the microwave reflection loss of **a** LSMO/wax compositions with different particle sizes ($d = 2$ mm) and **b** S35/wax compositions with different absorber thicknesses. Inset of **a** shows frequency dependence of the loss factor of S35/wax compositions

between the relative permittivity and permeability in materials. Either magnetic loss or dielectric loss may result in a weak EM wave absorption property due to the imbalance of the EM match [37]. Figure 4a shows the frequency dependence of the RL of LSMO/wax compositions with the same thickness 2 mm. It is clear that the position of RL peak maintain at ~ 8.2 GHz, the maximum values of RL are -8.56 , -10.57 , and -14.56 dB for S150, S100, and S35, respectively, increasing gradually with decreasing particle size. Obviously, the absorption bandwidth (RL < -10 dB) of S35 is broader than that of the others. In the case of the core/shell S35 nanoparticles, a better EM match is set up due to the existence of the protective amorphous shells and its particular core/shell microstructures, which resulting in a broadband absorption. Figure 4b shows the reflection loss of the S35/wax composite with different assumed thicknesses. It is found that the RL peaks move to the low frequency region with the increase in the absorber thickness. It is seen that the optimal RL reaches -41.1 dB at 8.2 GHz with a matching thickness of 2.2 mm. It is worth noting that the maximum values of RL of all the three samples are lower than -10 dB, and the RL values under -10 dB are obtained in the range of 5.5–11.3 GHz for absorber thicknesses of 1.5–2.5 mm. This frequency range (RL < -10 dB) is broader than

those excellent absorbers reported in the literatures, i.e., Ni/polyaniline nanocomposites [38], Fe(C) nanocapsule [39], $\text{La}_{1-x}\text{Sr}_x\text{MnO}_3$ powders [18]. Although the saturation magnetization of S35 nanoparticles is relatively lower, the special intrinsically core/shell microstructure of the nanoparticles with amorphous shell and ferromagnetic core is the vital factor for the above phenomenon.

The dielectric loss factor ($\tan \delta_\epsilon = \epsilon''/\epsilon'$) and the magnetic loss factor ($\tan \delta_\mu = \mu''/\mu'$) may well explain why S35 nanoparticles have such excellent microwave absorption properties in a very wide frequency range, as shown in the inset of Fig. 4a. It is found that the dielectric loss factor shows an approximately constant value around 0.05 with a slight fluctuation, whereas the values of the magnetic loss factor exhibits a gradual increase from 0.39 to 0.47 in 1–8.2 GHz and then decreases at higher frequencies. The steady dielectric loss in the whole frequency range proves the balanced EM matching in the composites, suggesting that the enhanced microwave absorption properties result from the cooperative effect of the amorphous shells and the ferromagnetic cores. That is to say, the amorphous shells play an important role in allowing broader frequency range microwave absorption because of their steady dielectric loss ability in this range. It is evident that the excellent microwave absorption properties for the intrinsically core/shell LSMO nanoparticles are a consequence of the better EM matching due to the existence of the protective amorphous shells, the ferromagnetic cores, as well as the particular core/shell microstructure.

Conclusions

In conclusion, intrinsically core/shell LSMO nanoparticles exhibit excellent microwave absorption properties. The analysis of experimental data shows that the optimal reflection loss reaches -41.1 dB at 8.2 GHz with a matching thickness of 2.2 mm, the bandwidth with a reflection loss less than -10 dB is obtained in the range of 5.5–11.3 GHz for absorber thicknesses of 1.5–2.5 mm, which are attributed to the electromagnetic match in microstructure, the strong natural ferromagnetic resonance, as well as the steady dielectric loss. The LSMO nanoparticles with amorphous shells and ferromagnetic cores may have potential applications in wide-band and effective microwave absorption materials.

Acknowledgments This work was supported by the National Key Basic Research under Contract Nos. 2007CB925001, 2007CB925002, the National Nature Science Foundation of China under Contract No. 10874051, and Anhui NSF Grant Nos. 070416233, KJ2007A084. The first author would like to thank Prof. Y. M. Zhang and Dr. M. P. Jin for their valuable discussion on this work.

References

1. A. Dutta, N. Gayathri, R. Ranganathan, *Phys. Rev. B* **68**, 054432 (2003)
2. S.A. Corr, Y.P. Rakovich, Y.K. Gun'ko, *Nanoscale Res. Lett.* **3**, 87 (2008)
3. V.B.regar, *IEEE Trans. Magn.* **40**, 1679 (2004)
4. J.L. Snoek, *Physica (Amsterdam)* **14**, 207 (1948)
5. S. Sugimotoa, T. Maedaa, D. Booka, T. Kagotania, K. Inomataa, M. Hommaa, H. Otab, Y. Houjou, R. Sato, *J. Alloy. Compd.* **330**, 301 (2002)
6. J. Liu, F. Liu, K. Gao, J. S. Wu, D.F. Xue, *J. Mater. Chem.* (2009) doi:[10.1039/b900116f](https://doi.org/10.1039/b900116f)
7. C.Q. Zhu, P. Wang, X. Wang, Y. Li, *Nanoscale Res. Lett.* **3**, 213 (2008)
8. G. Morello, M. Anni, P.D. Cozzoli, L. Manna, R. Cingolani, M.D. Giorgi, *Nanoscale Res. Lett.* **2**, 512 (2007)
9. M. Protière, P. Reiss, *Nanoscale Res. Lett.* **1**, 62 (2006)
10. C.L. Yan, D.F. Xue, *J. Phys. Chem. B* **110**, 25850 (2006)
11. C.L. Yan, D.F. Xue, *J. Phys. Chem. B* **110**, 7102 (2006)
12. J.R. Liu, M. Itoh, K. Machida, *Chem. Lett.* **32**, 394 (2003)
13. J.R. Liu, M. Itoh, K. Machida, *Appl. Phys. Lett.* **83**, 4017 (2003)
14. X.F. Zhang, X.L. Dong, H. Huang, Y.Y. Liu, W.N. Wang, X.G. Zhu, B. Lv, J.P. Lei, C.G. Lee, *Appl. Phys. Lett.* **89**, 053115 (2006)
15. R.C. Che, C.Y. Zhi, C.Y. Liang, X.G. Zhou, *Appl. Phys. Lett.* **88**, 033105 (2006)
16. F.J. Owens, *J. Appl. Phys.* **82**, 3054 (1997)
17. V.V. Srinivasu, S.E. Lofland, S.M. Bhagat, K. Ghosh, S.D. Tyagi, *J. Appl. Phys.* **83**, 2866 (1998)
18. G. Li, G.G. Hu, H.D. Zhou, *Mater. Chem. Phys.* **75**, 101 (2002)
19. K.S. Zhou, H. Xia, K.L. Huang, L.W. Deng, D. Wang, Y.P. Zhou, S.H. Gao, *Physica B* **404**, 175 (2009)
20. E.J. Vanzura, J.R. Baker-Jarvis, *IEEE Trans. Microwave Theory Tech.* **42**, 2063 (1994)
21. P.G. Radaelli, M. Marezio, H.Y. Hwang, S.W. Cheong, B. Batlogg, *Phys. Rev. B* **54**, 8992 (1996)
22. F. Gong, W. Tong, S. Tan, Y.H. Zhang, *Phys. Rev. B* **68**, 174410 (2003)
23. L. Zheng, K.B. Li, Y.H. Zhang, *Phys. Rev. B* **58**, 8613 (1998)
24. A. de Andrés, S. Taboada, J.L. Martínez, A. Salinas, J. Hernández, R. Sáez-Puche, *Phys. Rev. B* **47**, 14898 (1993)
25. T. Zhu, B.G. Shen, J.R. Sun, H.W. Zhao, W.S. Zhan, *Appl. Phys. Lett.* **78**, 3863 (2001)
26. L.I. Balcells, J. Fontcuberta, B. Martínez, X. Obradors, *Phys. Rev. B* **58**, R14697 (1998)
27. H. Cao, S.L. Suib, *J. Am. Chem. Soc.* **116**, 5334 (1994)
28. J.M. Yan, X.B. Zhang, S. Han, H. Shioyama, Q. Xu, *Angew. Chem. Int. Ed.* **47**, 2287 (2008)
29. S. Ramo, J.R. Whinnery, T.V. Duzer, *Fields and waves in communication electronics* (Wiley, New York, 1984)
30. K.S. Zhou, J.J. Deng, L.S. Yin, S.H. Ma, S.H. Gao, *Trans. Nonferrous Met. Soc. China* **17**, 947 (2007)
31. S.M. Abbas, R. Chatterjee, A.K. Dixit, A.B.R. Kumar, T.C. Goel, *J. Appl. Phys.* **101**, 074105 (2007)
32. C. Zener, *Phys. Rev.* **82**, 403 (1951)
33. V.V. Srinivasu, S.E. Lofland, S.M. Bhagat, K. Ghosh, S.D. Tyagi, *J. Appl. Phys.* **86**, 1067 (1999)
34. S.I. Patil, S.E. Lofland, Q.Q. Shu, S.M. Bhagat, *J. Appl. Phys.* **87**, 2652 (2000)
35. T. Zhang, G. Li, T. Qian, J.F. Qu, X.Q. Xiang, X.G. Li, *J. Appl. Phys.* **100**, 094324 (2006)
36. Y. Naito, K. Suetake, *IEEE Trans. Microwave Theory Tech* **MTT-19**, 65 (1971)
37. A. Wadhawan, D. Garrett, J.M. Perez, *Appl. Phys. Lett.* **83**, 2683 (2003)
38. X.L. Dong, X.F. Zhang, H. Huang, F. Zou, *Appl. Phys. Lett.* **92**, 013127 (2008)
39. X.F. Zhang, X.L. Dong, H. Huang, B. Lv, J.P. Lei, C.F. Choi, *J. Phys. D: Appl. Phys.* **40**, 5383 (2007)